ORIGINAL PAPER

Experimental Study on Mechanical and Strain Localisation Behaviour of Sandstone Under Seepage–Stress Coupling

Yian Chen[1] · Jiang Xu[1] · Qi Cao[1] · Haokui Rao[1] · Mengqin Cui[1] · Qianwen Zhang[1] · Shoujian Peng[1]

Abstract

In this study, the effects on the mechanical and seepage behaviour of sandstone were analysed using triaxial compression tests under various confining and seepage pressure conditions. Three-dimensional digital image correlation and scanning electron microscopy were used to monitor the strain localisation behaviour and microstructure of the sandstone under various conditions. The results show that the peak stress and peak permeability of sandstone are more sensitive to the confining pressure factor than to the seepage pressure factor. The amount of axial strain in the strain field was apparent and the sample became severely compressed as the confining pressure decreased. However, according to the statistical results of the axial strain values at the onset of localisation, the influence of the seepage pressure is more significant. The effect of seepage on the microstructure of the sandstone fracture surface mainly comprises the erosion of mineral debris produced by damage, which is marginally affected by the confining pressure. The results of this study can enhance the understanding of the role of water in the mechanical and strain localisation behaviour of sandstone.

Highlights

- A three-dimensional digital image correlation (3D-DIC) method was used to observe the strain field of sample surface in the triaxial compression tests.
- The mechanisms of confining and seepage pressure on the mechanical and seepage behaviours of sandstone were studied.
- The effects of seepage pressure on strain localisation characteristics were analysed.

1 Introduction

The fracture zones of rocks subjected to triaxial stress are concentrated. This phenomenon is more pronounced under seepage–stress coupling conditions. The elastic plasticity and inhomogeneity of rocks cause deformation localisation in a small area under loading conditions (Makhnenko et al. 2020). This process occurs continually during progressive rock failure. In geotechnical engineering, the phenomenon of strain localisation in the surrounding rock often determines collapse, leakage, and instability failure (Chen et al. 2021; Giot et al. 2018; Jeanpert et al. 2019; Li et al. 2020; Xue et al. 2021; Yu et al. 2019, 2020). Therefore, an experimental study on localisation behaviour is of considerable significance to the durability and stability of a rock.

The strain localisation behaviour of a rock can result from stress concentrations caused by complex stress conditions, including confining and seepage pressure (Chen et al. 2022; Erarslan 2021; Nanda et al. 2020). The existence of confining pressure can change the resultant force direction and transform the rock deformation from irregular to regular, based on rock mechanics (Chen et al. 2020; Tang et al. 2019). Traditional triaxial compression tests showed that a

✉ Shoujian Peng
sjpeng@cqu.edu.cn

[1] State Key Laboratory of Coal Mine Disaster Dynamics and Control, Chongqing University, Chongqing 400044, China

rock was damaged by a single fracture owing to shear. The strain increased at the fracture, and strain localisation was observed. Furthermore, the mechanisms based on which confining and seepage pressures affect a rock mechanical behaviour have been studied (Duda and Renner 2013; Eghbalian et al. 2021; Samuelson et al. 2009; Shilko et al. 2018; Wu 2020; Xie et al. 2021; Xue et al. 2020; Zhang et al. 2020). Seepage pressure affects the elasticity and brittleness of a rock by acting on pores, thus changing the mechanical properties of the rock. Crack propagation is accelerated by the prolonged chemical action of stress corrosion under low-stress conditions. The inflow of fluid affects the mechanical behaviour of the rock by changing the pore pressure and arrangement of the cementing material. According to the principle of effective stress (Delonca and Vallejos 2020), an increase in the internal pore pressure results in a decrease in the effective confining pressure and fluid flow resistance. Strain localisation behaviour is affected by both stress and seepage pressure, and it changes the evaluation of the unstable area of water-bearing strata (Lei et al. 2011; Makhnenko and Labuz 2015). Although the description and cause of strain localisation have been extensively studied in relation to stress concentration, the mechanism of strain localisation has rarely been determined based on quantitative analyses (Benallal and Comi 2003). This mechanism may play an important role in fracture behaviour and control the formation of damaged areas and intensification of fluid diffusion.

The three-dimensional (3D) digital image correlation (3D-DIC) method is often used in rock tests to quantify variations in the surface deformation field (Heinz and Wiggins 2010; Sutton et al. 2007). The results obtained using this method are similar to those obtained using an extensometer as this method has various advantages, including a lack of contact with the sample surface and the ability to monitor the entire area of the sample. This method uses image analysis to quantify small and extremely large strains after sample failure (Huang et al. 2020). To date, the DIC method has been extensively used to observe the strain fields on sample surfaces (Lv et al. 2021; Song et al. 2016; Xu et al. 2019; Zhou et al. 2019; Zhu et al. 2019). Compared with traditional strain measurement methods (such as the linear variable differential transformer), the 3D-DIC method can offset the effect of bedding error on the strain, a problem that the traditional method cannot solve (Munoz and Taheri 2017a). However, few studies have monitored the evolution of rock surface strain fields from various directions in triaxial compression tests.

The triaxial compression tests of sandstone samples were conducted under stress–seepage coupling conditions, and the processes of sample failure were monitored in this study using the 3D-DIC method. The influence of confining and seepage pressure on sandstone mechanical and strain localisation behaviour is discussed based on an analysis of the different forms of the strain and shear-stress fields on the rock surface during the progressive failure process. Furthermore, the 3D-DIC method was further used to analyse the changes in the strain inside and outside the localisation zone to investigate the formation mechanism of strain localisation.

2 Experimental Method

2.1 Sample Processing

The sandstone samples selected for this study were obtained from the banks of the Yangtze River in China. According to mineral analysis, the crystals in the sample were mainly those of quartz, albite, and potassium feldspar, and the cementation was composed of chlorite. Base on thin-section identification and analysis of the sandstone under a microscope, it was determined to possess a granular structure with an average size in the range of 0.05–0.10 mm. The sandstone was then processed into cylindrical samples with sizes set based on the recommendations of the International Society for Rock Mechanics (Munoz and Taheri 2017b). The primary samples were 25 mm in diameter and 50 mm in height, with variations in the flatness of the end surfaces being less than 0.02 mm. The basic physical and mechanical properties of the sample are listed in Table 1.

In addition, irregular speckles on the sample surface were required to be artificially generated to use the 3D-DIC method. The sample surface was coated with waterproof glue for better paint adhesion, which can prevent water from flowing out of the sample surface. Matte white and black paint were used to produce irregular speckles on the sample surface that could be identified using the 3D-DIC

Table 1 Basic physical and mechanical properties of sandstone sample

Rock type	Density (g/cm^3)	σ_{ucs} (MPa)	Young's modulus (GPa)	Poisson's ratio	Saturated water rate (%)	P-wave velocity (m/s)
Sandstone (average)	2.26	66.29	11.54	0.24	5.01	3113.24
	2.30	69.11	12.46	0.25	4.52	3256.72
	2.31	67.08	11.67	0.24	4.90	3144.75
	2.29	67.49	11.89	0.24	4.81	3171.57

method. The processed sample was filled with water using the vacuum water-saturation method; when its quality ceased to change, the sample was considered to have reached the fully saturated state. The water-filled sample was then loaded into the transparent pressure cell to conduct the triaxial compression test. A flowchart of the sample processing is shown in Fig. 1.

2.2 Experimental Setup

An independently developed triaxial compression experimental setup (Okubo et al. 2008) and a plunger pump that provided seepage pressure were used in the tests, as shown in Fig. 2. The loading system in the triaxial compression experimental setup provided stable axial stress and servo control, and the numerical value of the force could be relayed back to the control system in real time. The confining pressure in the triaxial confining chamber was provided by a hydraulic pump, and an accumulator was adopted to ensure the stability of the confining pressure. The seepage pressure was provided by a 260D plunger pump (Teledyne ISCO), which was connected to the end-face of the sample via a metallic pipe. The surface images of each sample were acquired from various angles using six high-resolution cameras installed in the 3D-DIC system. The parameters of these six cameras could be calibrated simultaneously, and their spatial coordinate system could be determined using the triangular prism coding calibration board (Munoz et al. 2016b). To facilitate this, the triaxial confining chamber was made of a transparent polymer material with high transmittance, and the surface crack propagation was captured using the 3D-DIC method. Changes in the sample surface at different times were detected reflected by the movement of speckles to obtain the evolution laws of various strain fields (Kahnjetter and Chu 1990; Lu et al. 1997).

2.3 Triaxial Compression Seepage Test

In this study, five test conditions were designed to analyse the influences of the confining and seepage pressures on sandstone strain localisation, as shown in Table 2. The test stress path with the samples labelled as C9-P8. is shown in Fig. 3. The axial stress was applied first, and it was followed by the applications of the confining, and seepage pressures (Munoz et al. 2016a). The certainty and repeatability of the mechanical and strain localisation behaviours of the sample were ensured by repeating the test three times. Seepage pressure was applied before the triaxial compression test to ensure that the sample had a stable pore pressure. The sample was then destroyed via axial displacement loading, and its mechanical behaviours and seepage characteristics were recorded during the failure process.

Darcy's law was applied to the calculation of rock permeability (Yang et al. 2015), as shown in Eq. (1), and the volumetric strain $\left(\varepsilon_v\right)$ was calculated using the axial $\left(\varepsilon_1\right)$ and radial $\left(\varepsilon_3\right)$ strains (Martin and Chandler 1994), as expressed by Eq. (2).

$$k = \frac{\mu V L}{A \Delta t p_w} \tag{1}$$

$$\varepsilon_v = \varepsilon_1 + 2\varepsilon_3 \tag{2}$$

Here, k is the permeability calculated by Darcy's law, m^2; μ is the dynamic viscosity coefficient of the fluid, $\mu = 1.005 \times 10^{-3}$ Pa·s; V is the flow rate of the fluid per

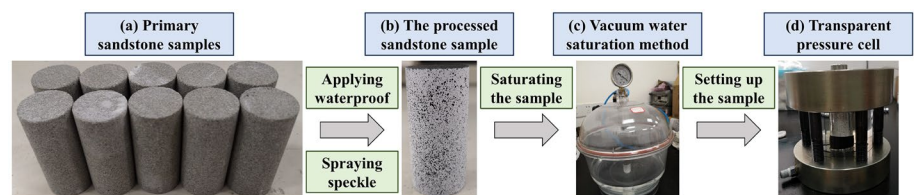**Fig. 1** Sandstone sample processing flowchart

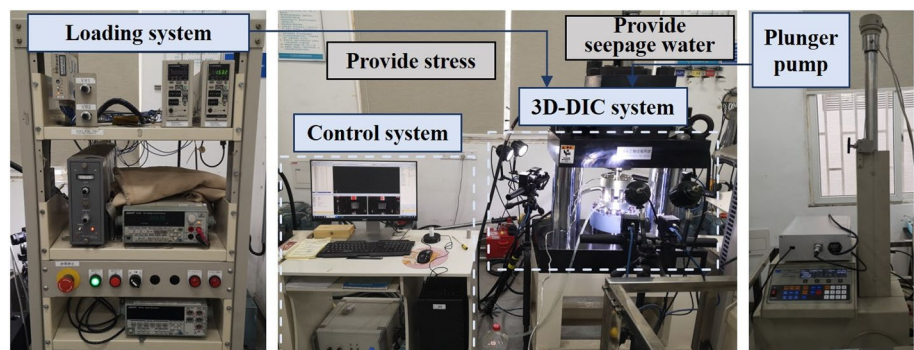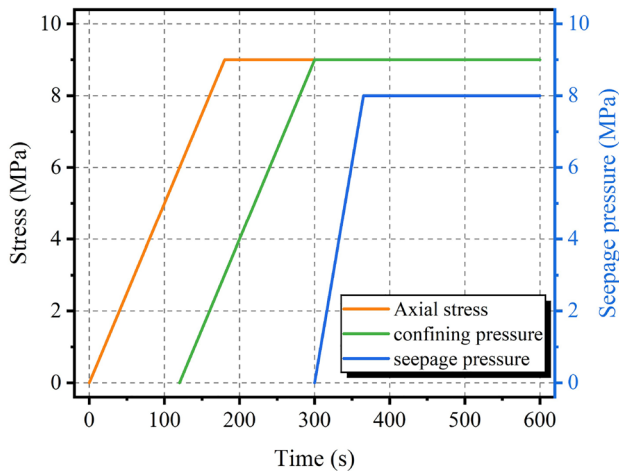**Fig. 2** Photographs of the experimental setup

Table 2 Experimental conditions used in this study

Rock types	Axial loading rate (mm/s)	Confining pressure (MPa)	Seepage pressure (MPa)	Sample label
Sandstone	5×10^{-4}	9.0	8.0	C9-P8
			5.0	C9-P5
			2.0	C9-P2
		6.0	5.0	C6-P5
			2.0	C6-P2
			0.0	C6-P0
		3.0	2.0	C3-P2

Fig. 3 Stress path under the conditions of a 9.0 MPa confining pressure and an 8.0 MPa seepage pressure

second, m^3; L is the distance covered by the fluid flowing through the sample, m; A is the area of the fluid flowing through the sample, m^2; Δt is a specific time interval, s; and p_w is the seepage pressure difference between the fluid entering the sample and leaving the sample, Pa.

3 Experimental Results

3.1 Mechanical and Seepage Behaviours of Sandstone

Figure 4 shows the effective axial stress–strain and permeability–axial strain curves of the sandstone under different conditions. The data of axial and radial strains during the progressive failure process of the sample were obtained by the 3D-DIC system. The process of sandstone triaxial compression undergoes five stages under seepage–stress coupling conditions.

The primary pores in the sandstone under the loading condition are gradually compressed; however, this stage is not evident in the stress–axial strain curve. This may be because the seepage pressure results in a stable pore-water pressure in the fully saturated sandstone, thus causing the pores to resist compression effectively in the initial loading stage. Sandstone exhibits linear elastic mechanical properties within its load-bearing capacity range.

At the end of the linear elastic stage, ordered cracks appeared in the sample, and the sample began to expand gradually. After the yield point, the cracks in the sample began to expand in a disordered fashion, and the sample volume changed from the compression to the expansion state. The sample could not bear more amount of effective axial stress at the peak strength and produced a macro fracture, and the effective axial-stress level was reduced to the residual strength level.

The pore state of sandstone can be analysed based on permeability changes. The continuous decrease in permeability indicates that the number of seepage channels in the sandstone decreased, and new cracks formed more seepage channels; this led to an increase in permeability. Permeability was maximised after the peak stress because the sandstone was not completely fractured at the peak stress and a complete seepage channel being formed.

According to the mechanical and seepage behaviours of sandstone, five representative time points were selected to analyse the evolution law of the displacement and strain fields on the surfaces of the samples. Point A was the initial point of the test, point B was located at the instant the stress level was 50% of the peak stress (before the peak stress), point C was located at the peak-stress instant, point D was located at the peak-permeability instant, and point E was located at the residual strength instant.

Figure 5 shows the statistics of peak effective axial stress and peak permeability of the sandstone under various conditions. The projection at the bottom part in Fig. 5a shows that the peak strength of the sandstone decreased as the seepage pressure increased or the confining pressure decreased. The sensitivity of sandstone peak stress to the confining pressure was higher than that to seepage pressure. The projection at the bottom part in Fig. 5b shows that the peak permeability of the sandstone increased as the seepage pressure increased, or as the confining pressure decreased. The peak
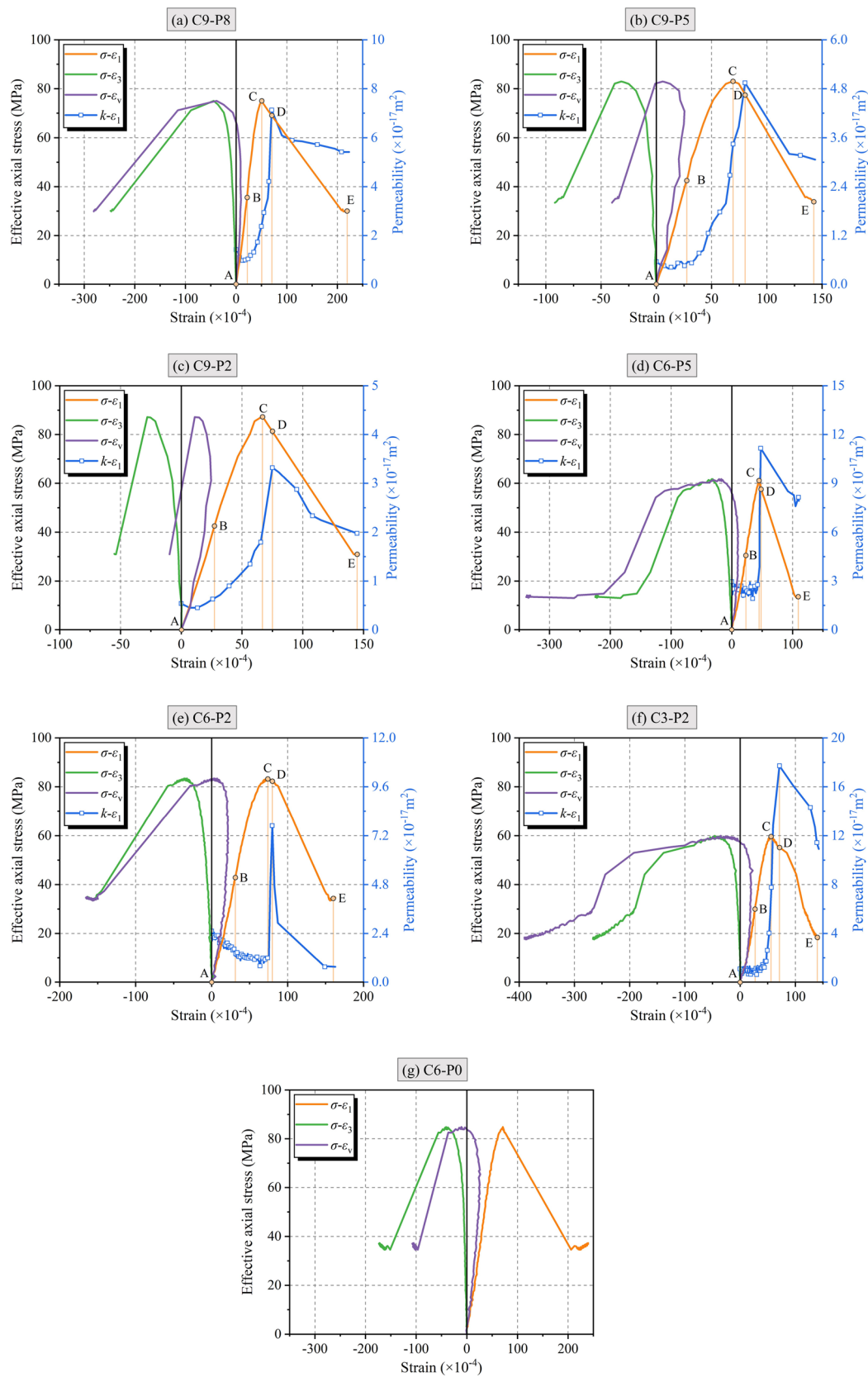
Fig. 4 Effective axial stress–strain and permeability–axial-strain curves for sandstone under various conditions
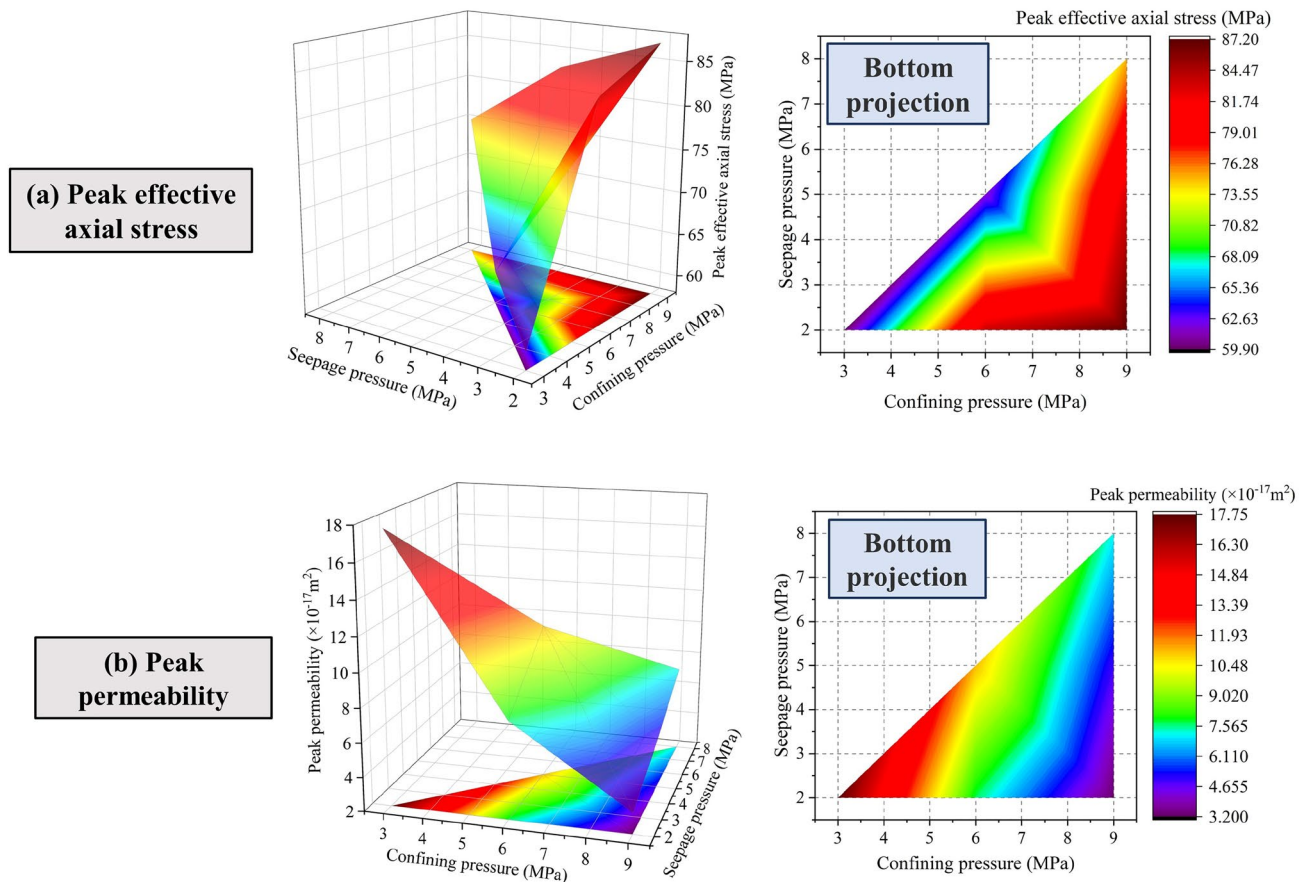
Fig. 5 Surface diagram of peak stress and peak permeability for sandstone under various conditions

permeability of the sandstone was affected more by the confining pressure. This indicates that confining pressure plays an important role in the mechanical behaviour and seepage characteristics of sandstone. The ductility and degree of pore compression of sandstone increased when subjected to high confining pressures, thus strengthening its bearing capacity and imperviousness. Seepage pressure can weaken the cementation in sandstone and reduce the cohesiveness and strength of the sample. The high seepage pressure increased the pore pressure inside the sample and enabled the water molecules to enter the junctions between crystals and cementations more easily, thus impairing intergranular connections. The confining pressure changed the stress state of the sample from unidirectional to multidirectional, whereas the seepage pressure, which acted on the end-face and internal pores of the sample, could partially offset the confining pressure. Therefore, when considering the stability of the sandstone, more attention should be paid to the effects of the confining pressure.

3.2 Evolution Law of Surface Displacement and Strain Field

The progressive failure of the sample under seepage–stress coupling was monitored using the 3D-DIC system. Figure 6 illustrates the evolution law of the axial strain field on the sample surfaces under various conditions. The sample surface axial strain field at point A was located at the initial moment of the test and was used as the reference. The strain fields have the same colour at point A, thus indicating that the initial axial strain value was zero under various conditions. The sandstone was in the linear elastic stage at point B, and the axial strain field appeared as a randomly distributed green pattern, indicating that the entire sample was compressed when subjected to axial stress. In the same reference legend, the axial strain variation became more evident as the confining pressure decreased; during this period, the sample was compressed more. The maximum bearing capacity of the sample was reached at point C. Compared with the axial strain at point B, the sample produced a greater axial strain at point C. Although the crack propagation inside the sandstone was prominent, no obvious deformation occurred
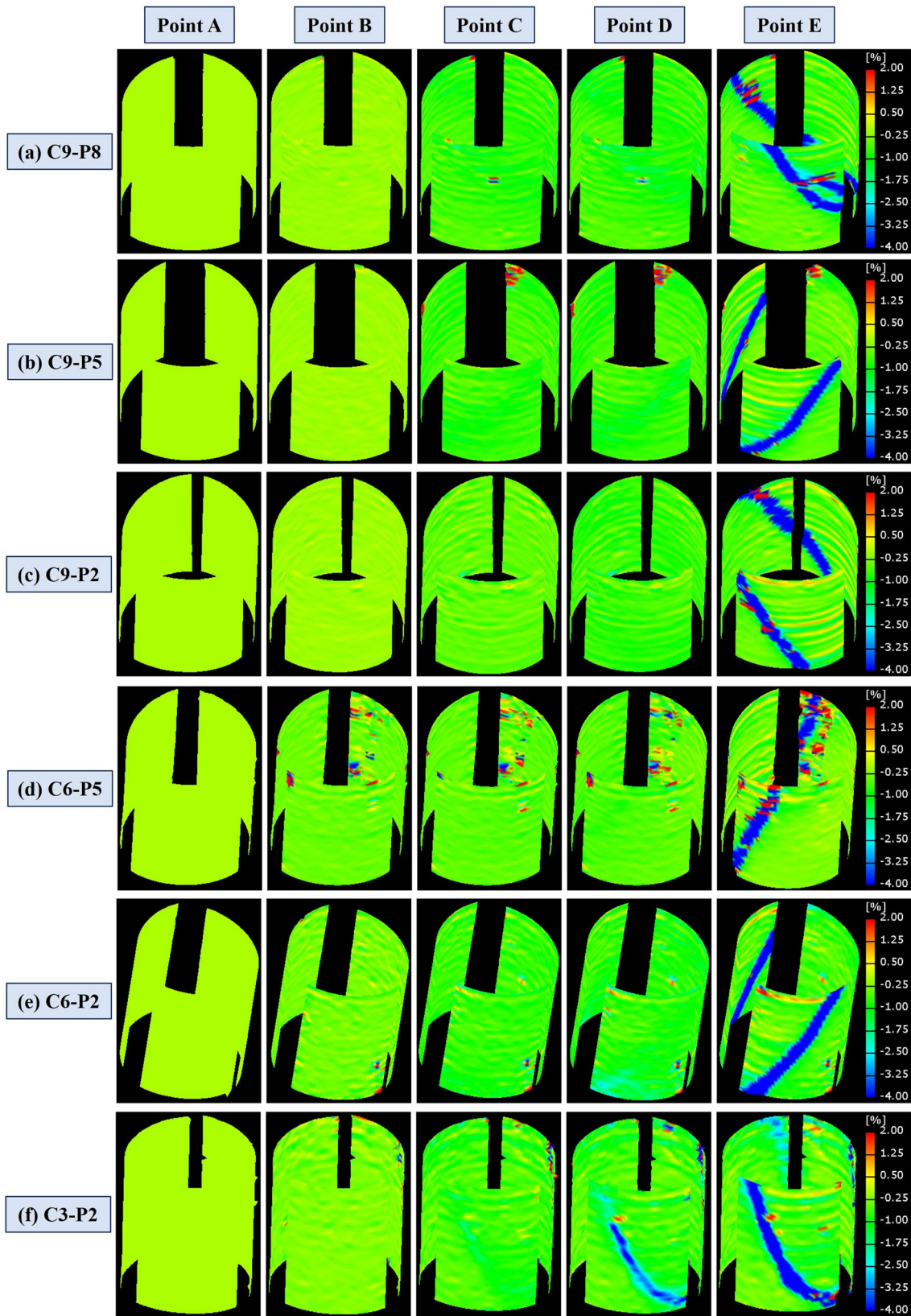
Fig. 6 Evolution of the axial strain field on the sample surface under various conditions

on the sample surface. A light blue region exists in the axial strain field (sample label C3-P2), and deformation and fracture occurred in this region. This suggests that the lower the confining pressure, the stronger the counteracting effect of seepage pressure, and earlier the sandstone fracture. Cracks began to appear on the sample surface at point D. The permeability values indicate that the flow of seepage channels in the sample reached the maximum at this instant. A macroscopic fracture appeared at the residual strength (point E), where the large axial strain deformation region was concentrated, and strain localisation behaviour appeared. The macroscopic fracture on the sample surface extended from the previous cracks and exhibited a consistent trend in the evolution of the axial strain field. The increase in seepage pressure changed the direction of crack propagation according to the microstructure of the axial strain's localisation region. In the traditional triaxial compression test, the fracture on the sandstone sample surface was a single inclined fracture. In the lower part of the sample, the effects of seepage pressure became less prominent and the radial force increased; this resulted in a change in the stress pattern at the tip of the crack owing to the seepage pressure distribution. Therefore, the crack ending exhibited a trend of radial propagation in the progressive failure process.

Figures 7 and 8 show the evolution of the radial strain and axial displacement fields, respectively, on the sample surface. Strain localisation behaviour also occurred in the radial strain field of the damaged sandstone, and the large

deformation region of the radial strain was the same as that of the axial strain; both of these regions were located at the macroscopic fracture. The axial displacement field on the sample surface exhibited variations, thus indicating that the penetrating crack divided the sample into two parts, namely residual and damaged. The damaged part slipped along the fracture surface direction and produced a large displacement owing to the direct action of the axial force. The residual part remained stable and produced minor displacements when subjected to the combined action of confining pressure and friction. The confining pressure improved the strength of the sample; this resulted in a larger displacement of the damaged part under high confining pressure conditions. When macroscopic cracks appeared, the influences of the confining pressure and axial stress were weakened by the seepage pressure acting on the fracture surface. This led to a smaller displacement of the damaged part when subjected to high seepage pressure.

4 Analysis and Discussion

4.1 Strain Localisation of Sandstone

The phenomenon of strain localisation is caused by drastic changes in the local strain owing to the stress concentration (Munoz and Taheri 2019). The sandstone sample produced a strain localisation zone when subjected to triaxial stress,
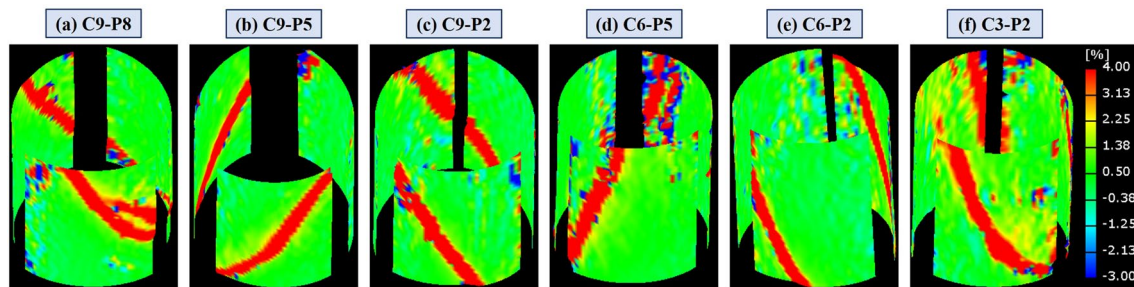

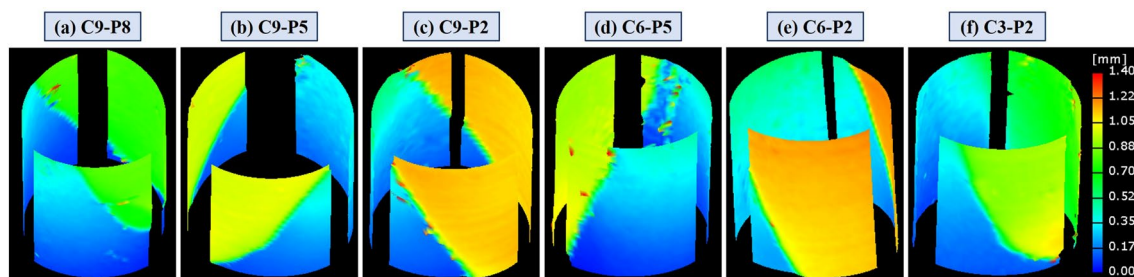**Fig. 7** Evolution of the radial strain field on the sample surface under various conditions

Fig. 8 Evolution of the axial displacement field on the sample surface under various conditions

which occurred separately from the failure of the sample. The findings on the formation process of the strain localisation zone can be used to analyse the failure mode and aid in predicting the range of sandstone failure areas. The 3D-DIC system was used to deploy virtual extensometers (VEs) to measure the strain variation in the corresponding area. Figure 9 shows the layout of the VEs on the main fracture surface of the sample. To monitor accurately the evolution law of strain localisation, three VEs of the same length were arranged inside and outside the strain localisation zone. Meanwhile, the axial and radial strain average data of the sample were obtained by VE3 and VE6, respectively, and were compared with the data inside and outside the strain localisation zone.

The measured data of the radial strain obtained by the VEs under various conditions are shown in Fig. 10. The curves begin to diverge at the peak stress, thus indicating the initiation of radial strain localisation. When the bearing capacity of the sandstone was exceeded, the radial strain in the localisation zone increased rapidly, whereas the strain outside the strain localisation zone remained unchanged, and the radial strain decreased in the residual strength stage.

Figure 11 shows the axial strain data measured by the VEs and the evolution of the difference of the axial strain inside and outside the strain localisation zone as a function of the average axial strain under various conditions. Unlike the radial strain localisation, the axial strain localisation occurred after the peak stress and axial strain outside the localisation zone decreased. This indicates that elastic deformation mainly occurred in the non-stress concentration zone during the loading process of the sample, whereas fracture in the strain localisation zone was due to stress overload. Many micro-cracks in the stress concentration zone were connected to form macro-cracks, the axial strain increased rapidly, and the non-stress concentration zone in the sandstone released elastic energy to the fracture, leading to an

increase in the rate of the crack propagation. Furthermore, the difference between the axial strain values inside and outside the axial strain localisation zone and average axial strain values was calculated. The difference between VE1 and VE3 increased gradually during stress loading, whereas the difference between VE2 and VE3 decreased gradually. When an obvious distinction exists between the two difference values, axial strain localisation is considered to occur.

The starting axial-strain values under various conditions are shown in Fig. 12. As shown, the strain values decrease when the seepage pressure increases or when the confining pressure decreases. The early occurrence of axial strain localisation is promoted by the seepage pressure. This means that when the sandstone is subjected to higher seepage pressures, it is more likely to fracture at smaller deformations. The crystals in sandstone do not readily melt in water, whereas the strength of cementation is susceptible to water. The confining pressure can only improve the bearing capacity of cementation in a limited manner. Under the condition of high seepage pressure, cementation is not only weakened by water but also dispersed by high pore pressure. The strength of cementation is one of the components of the cohesive force in sandstone, and its reduction leads to the failure of the sample in advance. Therefore, the initiation axial strain of the localisation zone is more sensitive to seepage pressure than to confining pressure.

4.2 Microcosmic Analysis of Sandstone Fracture Surface

The sandstone fracture surfaces were monitored using a scanning electron microscope under various conditions, as shown in Fig. 13. Figure 13a shows the crystal structure mainly present on the fractured surface, where cementation was washed away under high-seepage pressure conditions. The crystal was severely damaged, and a large number of transgranular cracks occurred under strong seepage–stress coupling conditions. The fractured surface appears as a mirror-shaped area, the microstructure is neat, and only a small amount of detrital mineral exists. The high pore pressure between the crystals also caused a large number of inter-crystalline cracks. Figure 13b shows the presence of spray-shaped areas on the fractured surface, which were formed by the impact of seepage pressure on the cementation bonded to the crystal. The residual detrital minerals on the fractured sandstone surface are shown in Fig. 13c. The pore pressure caused by the low-seepage pressure was less than the cohesive force of the detrital minerals; accordingly, the fluid could not wash away all debris and cementations, and the transgranular cracks were imperceptible. The microstructure of the fractured sandstone surface shown in Fig. 13d is similar to that shown in Fig. 13a, and it exhibits a mirror-shaped area and evident
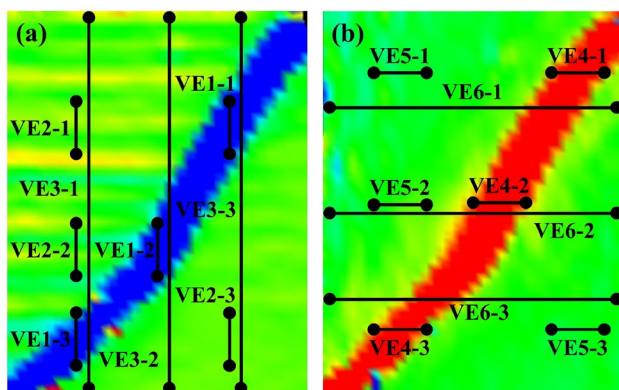

Fig. 9 Locations of **a** axial strain and **b** radial strain of virtual extensometers on the main fracture surface
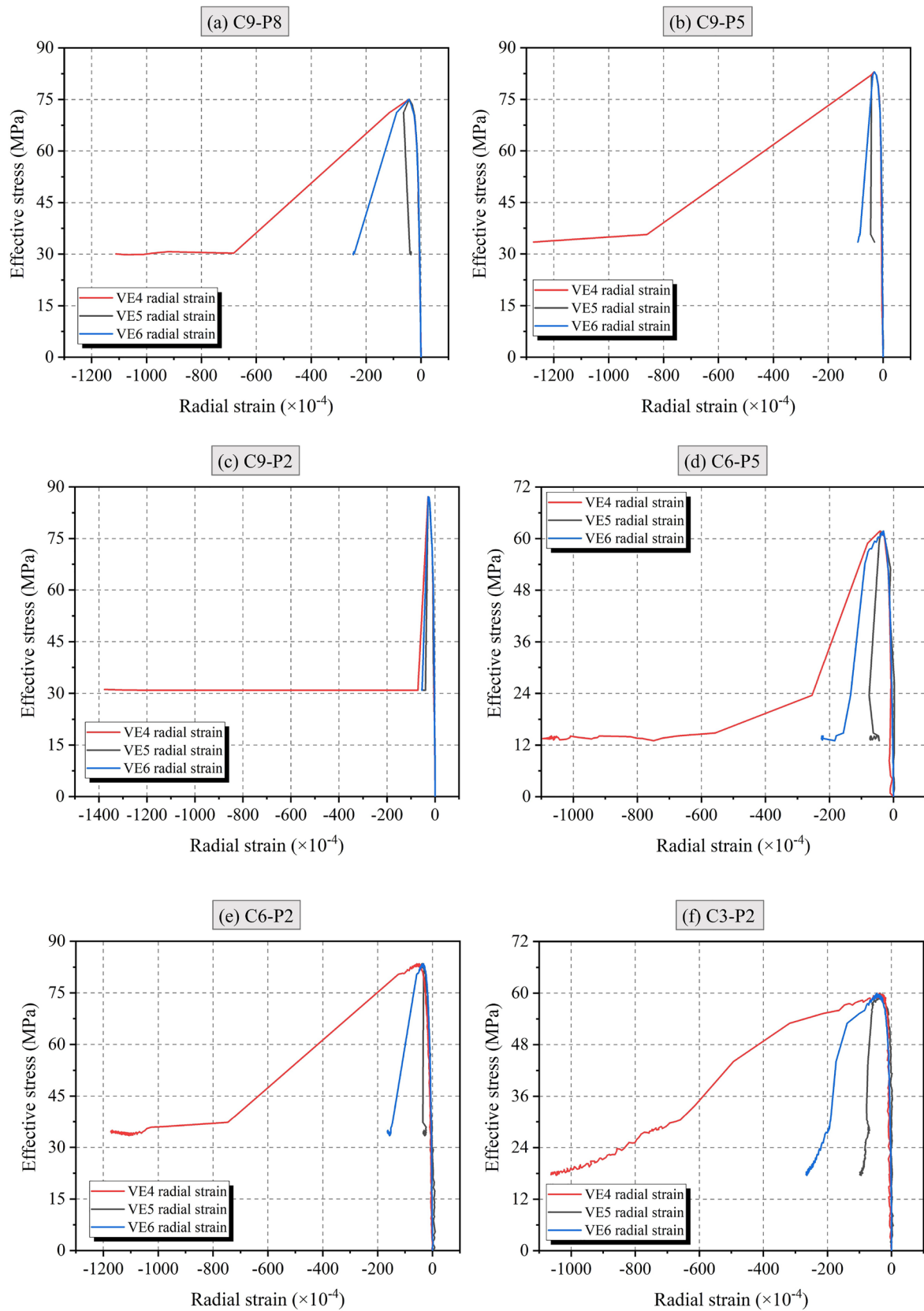
Fig. 10 Effective stress–radial strain curves for virtual extensometers (VE4, VE5, and VE6) under various conditions
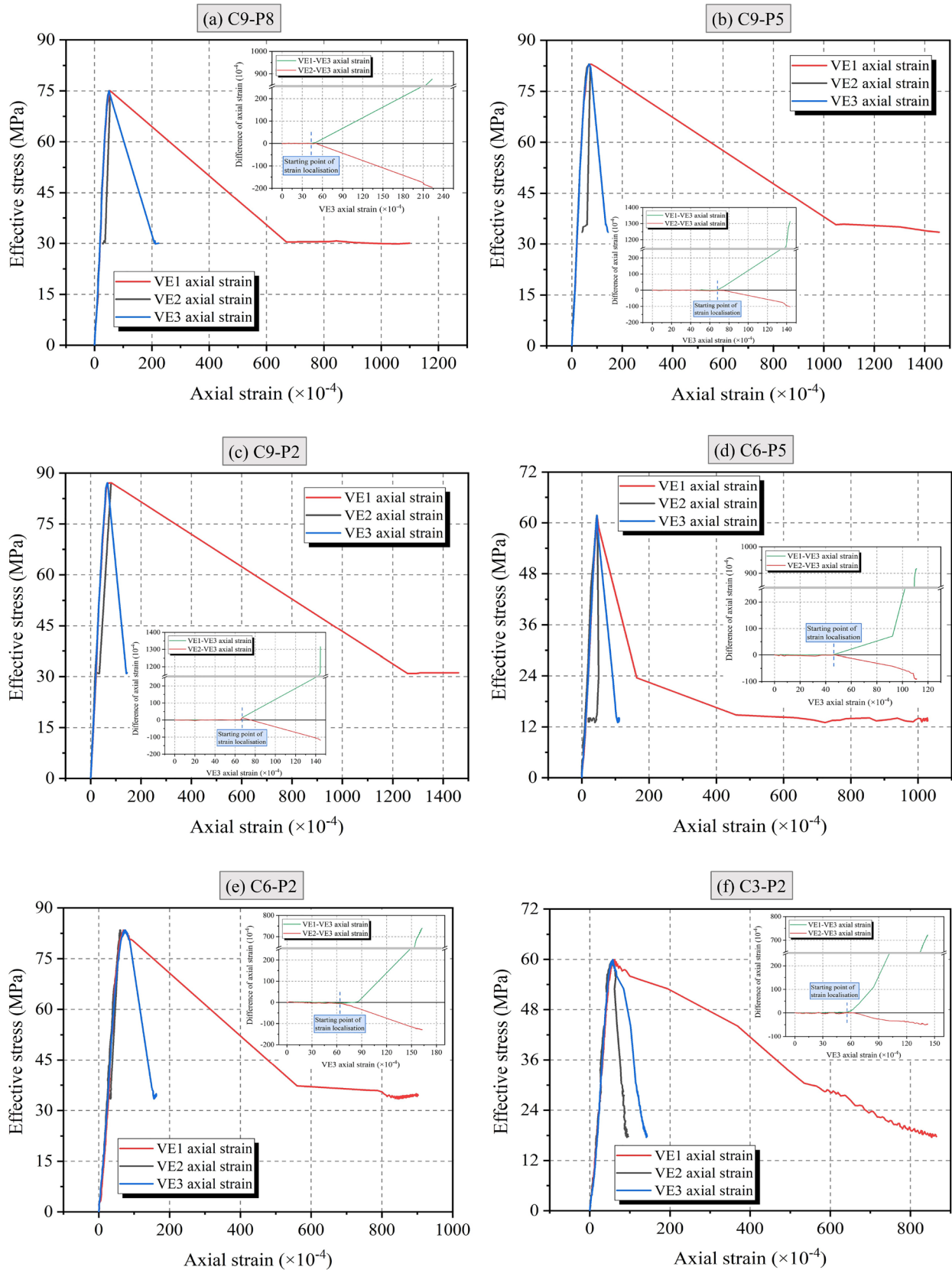
Fig. 11 Effective stress–radial strain curves for virtual extensometers (VE1, VE2, and VE3) and the evolution of the difference of the axial strain inside and outside the strain localisation zone with average axial strain under various conditions
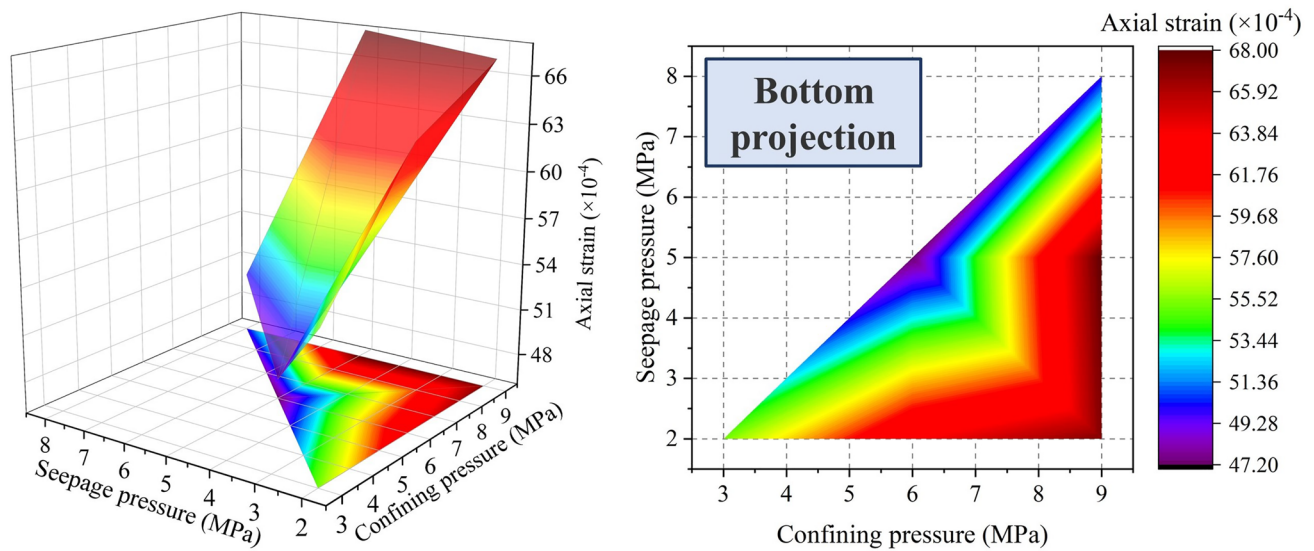
Fig. 12 Surface diagram of axial strain values at the initiation of localisation starting in sandstone under various conditions
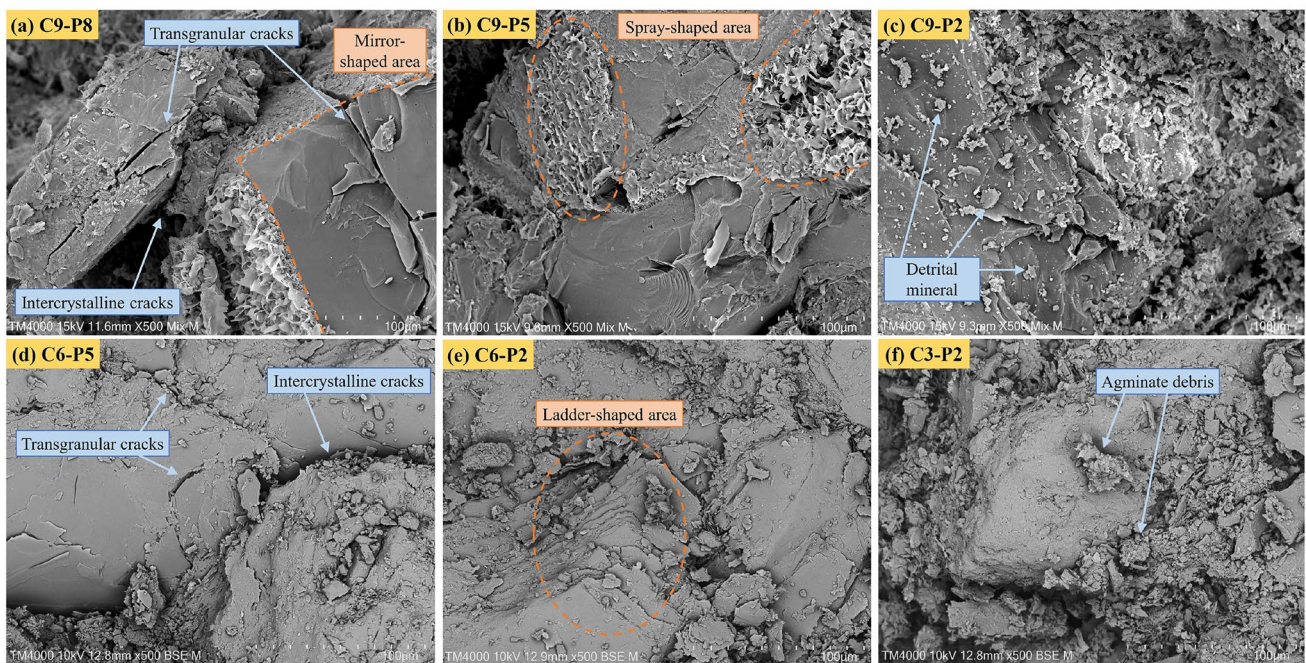

Fig. 13 Microstructures in the scanning electron microscopy image of the fractured sandstone surface under various conditions

transgranular cracks. The ladder-shaped area appears in Fig. 13e because of the incomplete scouring action of the seepage pressure. The microstructure of the fractured surface shown in Fig. 13f contains a large amount of agminate debris because the debris cannot be crushed under low confining and seepage pressures. The microstructure of the fractured surface of sandstone was clear, and the crystals were severely damaged when subjected to high seepage

and confining pressures, whereas a considerable amount of detrital minerals and agminate debris existed on the fractured sandstone surface under low-seepage–stress coupling conditions. These findings indicate that the effects of seepage pressure on the microstructure of the fractured sandstone surface were mainly concentrated on the erosion of minerals and debris produced by cracking, which was not affected by the confining pressure.

5 Conclusions

The effects of confining and seepage pressures on the mechanical and strain localisation behaviours, seepage characteristics, and microstructure of a fractured surface were studied. Additionally, the strain localisation behaviour in the progressive failure process of sandstone was analysed using the 3D-DIC method. The results can strengthen the understanding of the influence of water on the sandstone fracture mode. The conclusions are as follows:

1. Both the confining and seepage pressures can affect the bearing capacity and permeability of sandstone. The permeability first decreases and then increases during the sample loading process, and the time of peak permeability lags behind that of peak stress. However, the changes in peak stress and permeability are more sensitive to confining pressure than to seepage pressure because the seepage pressure can only offset a part of the influence of the confining pressure.

2. The sandstone fracture surface exhibited shear failure under seepage–stress coupling conditions. The end-part of the fracture showed a radial propagation trend when the seepage pressure value was close to the confining pressure value, and the damaged part of the sample produced a larger displacement along the fractured surface when subjected to a high confining pressure. This is because the stress mode at the crack tip is changed by the distribution of seepage pressure. The effect of seepage pressure on the microstructure of fractured sandstone surfaces mainly constitutes focuses on the erosion of minerals and debris produced by cracking.

3. Strain localisation behaviour results from stress concentration, and the axial strain localisation occurs after the peak stress, where the axial strain outside the localisation zone decreases. The non-stressed concentration zone in the sample releases elastic energy to the fracture and accelerates crack propagation. The initiation of axial strain in the localisation zone is more strongly affected by the seepage pressure.

Data Availability The raw/processed data required to reproduce these findings cannot be shared at this time as the data also forms part of an ongoing study.

Declarations

Conflict of interest The authors declare that they have no known competing financial interests or personal relationships that could have appeared to influence the work reported in this paper.

References

Benallal A, Comi C (2003) Perturbation growth and localization in fluid-saturated inelastic porous media under quasi-static loadings. J Mech Phys Solids 51:851–899. https://doi.org/10.1016/S0022-5096(02)00143-6

Chen CC, Xu J, Okubo S, Peng SJ (2020) Damage evolution of tuff under cyclic tension-compression loading based on 3D digital image correlation. Eng Geol. https://doi.org/10.1016/j.enggeo.2020.105736

Chen YA, Xu J, Peng SJ, Jiao F, Chen CC, Xiao ZY (2021) Experimental study on the acoustic emission and fracture propagation characteristics of sandstone with variable angle joints. Eng Geol. https://doi.org/10.1016/j.enggeo.2021.106247

Chen YA, Xu J, Peng SJ, Zhang QW, Chen CC (2022) Strain localisation and seepage characteristics of rock under triaxial compression by 3D digital image correlation. Int J Rock Mech Min. https://doi.org/10.1016/j.ijrmms.2022.105064

Delonca A, Vallejos JA (2020) Incorporating scale effect into a failure criterion for predicting stress-induced overbreak around excavations. Int J Rock Mech Min. https://doi.org/10.1016/j.ijrmms.2020.104213

Duda M, Renner J (2013) The weakening effect of water on the brittle failure strength of sandstone. Geophys J Int 192:1091–1108. https://doi.org/10.1093/gji/ggs090

Eghbalian M, Pouragha M, Wan R (2021) A three-dimensional multi-scale damage-poroelasticity model for fractured porous media. Int J Numer Anal Met 45:585–630. https://doi.org/10.1002/nag.3170

Erarslan N (2021) Experimental and numerical investigation of plastic fatigue strain localization in brittle materials: an application of cyclic loading and fatigue on mechanical tunnel boring technologies. Int J Fatigue. https://doi.org/10.1016/j.ijfatigue.2021.106442

Giot R, Auvray C, Conil N, de la Vaissiere R (2018) Multi-stage water permeability measurements on claystone by steady and transient flow methods. Eng Geol 247:27–37. https://doi.org/10.1016/j.enggeo.2018.10.019

Heinz SR, Wiggins JS (2010) Uniaxial compression analysis of glassy polymer networks using digital image correlation. Polym Test 29:925–932. https://doi.org/10.1016/j.polymertesting.2010.08.001

Huang F, Wu CZ, Ni PP, Wan GQ, Zheng AC, Jang BA, Karekal S (2020) Experimental analysis of progressive failure behavior of rock tunnel with a fault zone using non-contact DIC technique. Int J Rock Mech Min. https://doi.org/10.1016/j.ijrmms.2020.104355

Jeanpert J, Iseppi M, Adler PM, Genthon P, Sevin B, Thovert JF, Dewandel B, Join JL (2019) Fracture controlled permeability of ultramafic basement aquifers. Inferences from the Koniambo massif. New Caledonia Eng Geol 256:67–83. https://doi.org/10.1016/j.enggeo.2019.05.006

Kahnjetter ZL, Chu TC (1990) 3-Dimensional displacement measurements using digital image correlation and photogrammic analysis. Exp Mech 30:10–16. https://doi.org/10.1007/Bf02322695

Lei XL, Tamagawa T, Tezuka K, Takahashi M (2011) Role of drainage conditions in deformation and fracture of porous rocks under triaxial compression in the laboratory. Geophys Res Lett. https://doi.org/10.1029/2011gl049888

Li LP, Sun SQ, Wang J, Yang WM, Song SG, Fang ZD (2020) Experimental study of the precursor information of the water inrush in shield tunnels due to the proximity of a water-filled cave. Int J Rock Mech Min. https://doi.org/10.1016/j.ijrmms.2020.104320

Lu H, Vendroux G, Knauss WG (1997) Surface deformation measurements of a cylindrical specimen by digital image correlation. Exp Mech 37:433–439. https://doi.org/10.1007/Bf02317310

Lv XF, Yang YH, Chen Y, Wang NAJ, Yang M, Shao Y, Li JX (2021) Experimental study on the relationship between compression stability and deformation localization of viscous/brittle rock-like

materials. Adv Mater Sci Eng. https://doi.org/10.1155/2021/7153661

Makhnenko RY, Labuz JF (2015) Dilatant hardening of fluid-saturated sandstone. J Geophys Res Sol Ea 120:909–922. https://doi.org/10.1002/2014jb011287

Makhnenko RY, Ge CW, Labuz JF (2020) Localization of deformation in fluid-saturated sandstone. Int J Rock Mech Min. https://doi.org/10.1016/j.ijrmms.2020.104455

Martin CD, Chandler NA (1994) The progressive fracture of lac du bonnet granite. Int J Rock Mech Min 31:643–659. https://doi.org/10.1016/0148-9062(94)90005-1

Munoz H, Taheri A (2017a) Local damage and progressive localisation in porous sandstone during cyclic loading. Rock Mech Rock Eng 50:3253–3259. https://doi.org/10.1007/s00603-017-1298-8

Munoz H, Taheri A (2017b) Specimen aspect ratio and progressive field strain development of sandstone under uniaxial compression by three-dimensional digital image correlation. J Rock Mech Geotech 9:599–610. https://doi.org/10.1016/j.jrmge.2017.01.005

Munoz H, Taheri A (2019) Postpeak deformability parameters of localized and nonlocalized damage zones of rocks under cyclic loading. Geotech Test J 42:1663–1684. https://doi.org/10.1520/gtj20170266

Munoz H, Taheri A, Chanda EK (2016a) Fracture energy-based brittleness index development and brittleness quantification by pre-peak strength parameters in rock uniaxial compression. Rock Mech Rock Eng 49:4587–4606. https://doi.org/10.1007/s00603-016-1071-4

Munoz H, Taheri A, Chanda EK (2016b) Pre-peak and post-peak rock strain characteristics during uniaxial compression by 3D digital image correlation. Rock Mech Rock Eng 49:2541–2554. https://doi.org/10.1007/s00603-016-0935-y

Nanda K, Vaishakh TK, Das A, Misra S (2020) Hydro-mechanical response in porous rocks during localized deformation: finite element analysis. J Struct Geol. https://doi.org/10.1016/j.jsg.2019.103909

Okubo S, Fukui K, Hashiba K (2008) Development of a transparent triaxial cell and observation of rock deformation in compression and creep tests. Int J Rock Mech Min 45:351–361. https://doi.org/10.1016/j.ijrmms.2007.05.006

Samuelson J, Elsworth D, Marone C (2009) Shear-induced dilatancy of fluid-saturated faults: experiment and theory. J Geophys Res Sol Ea. https://doi.org/10.1029/2008jb006273

Shilko EV, Dimaki AV, Psakhie SG (2018) Strength of shear bands in fluid-saturated rocks: a nonlinear effect of competition between dilation and fluid flow. Sci Rep UK. https://doi.org/10.1038/s41598-018-19843-8

Song HP, Zhang H, Fu DH, Zhang Q (2016) Experimental analysis and characterization of damage evolution in rock under cyclic loading. Int J Rock Mech Min 88:157–164. https://doi.org/10.1016/j.ijrmms.2016.07.015

Sutton MA, Yan JH, Deng XM, Cheng CS, Zavattieri P (2007) Three-dimensional digital image correlation to quantify deformation and crack-opening displacement in ductile aluminum under mixed-mode I/III loading. Opt Eng. https://doi.org/10.1117/1.2741279

Tang Y, Okubo S, Xu J, Peng SJ (2019) Progressive failure behaviors and crack evolution of rocks under triaxial compression by 3D digital image correlation. Eng Geol 249:172–185. https://doi.org/10.1016/j.enggeo.2018.12.026

Wu X (2020) Crack initiation and failure mechanism of granite with single crack. Geotech Geol Eng 38:651–661. https://doi.org/10.1007/s10706-019-01053-2

Xie N, Tang HM, Yang JB, Jiang QH (2021) Damage evolution in dry and saturated brittle sandstone revealed by acoustic characterization under uniaxial compression. Rock Mech Rock Eng. https://doi.org/10.1007/s00603-021-02716-4

Xu W, Li JR, Zhang BY, Yang LX (2019) A new approach to reduce springback in sheet metal bending using digital image correlation. Int J Mater Res 110:726–733. https://doi.org/10.3139/146.111799

Xue J, Hao SW, Yang R, Wang P, Bai YL (2020) Localization of deformation and its effects on power-law singularity preceding catastrophic rupture in rocks. Int J Damage Mech 29:86–102. https://doi.org/10.1177/1056789519857121

Xue YG, Zhou BH, Li SC, Qiu DH, Zhang K, Gong HM (2021) Deformation rule and mechanical characteristic analysis of subsea tunnel crossing weathered trough. Tunn Undergr Sp Tech. https://doi.org/10.1016/j.tust.2021.103989

Yang SQ, Huang YH, Jiao YY, Zeng W, Yu QL (2015) An experimental study on seepage behavior of sandstone material with different gas pressures. Acta Mech Sin Prc 31:837–844. https://doi.org/10.1007/s10409-015-0432-7

Yu CY, Tang SB, Tang CA, Duan D, Zhang YJ, Liang ZZ, Ma K, Ma TH (2019) The effect of water on the creep behavior of red sandstone. Eng Geol 253:64–74. https://doi.org/10.1016/j.enggeo.2019.03.016

Yu J, Yao W, Duan K, Liu XY, Zhu YL (2020) Experimental study and discrete element method modeling of compression and permeability behaviors of weakly anisotropic sandstones. Int J Rock Mech Min. https://doi.org/10.1016/j.ijrmms.2020.104437

Zhang H, Zhao HB, Li WP, Yang XL, Wang T (2020) Influence of local frequent dynamic disturbance on micro-structure evolution of coal-rock and localization effect. Nat Resour Res 29:3917–3942. https://doi.org/10.1007/s11053-020-09683-7

Zhou XP, Zhang JZ, Qian QH, Niu Y (2019) Experimental investigation of progressive cracking processes in granite under uniaxial loading using digital imaging and AE techniques. J Struct Geol 126:129–145. https://doi.org/10.1016/j.jsg.2019.06.003

Zhu QQ, Li DY, Han ZY, Li XB, Zhou ZL (2019) Mechanical properties and fracture evolution of sandstone specimens containing different inclusions under uniaxial compression. Int J Rock Mech Min 115:33–47. https://doi.org/10.1016/j.ijrmms.2019.01.010